Elastic FWI for 3D and 4D subsalt imaging

Zedong Wu[1], Zhiyuan Wei[1], Zhigang Zhang[1], Jiawei Mei[1], Rongxin Huang[1], and Ping Wang[1]

https://doi.org/10.1190/tle44050372a1.1

Abstract

Full-waveform inversion (FWI) has found great success in different geologic settings and has become a must-have tool for velocity model building (VMB), particularly in salt environments where geology and velocity are often highly complex. While still acoustic, FWI has already significantly improved salt models and marked a step change in subsalt imaging compared to conventional VMB workflows driven by manual salt interpretation. Furthermore, the introduction of an innovative imaging method — FWI imaging — has delivered another step change in subsalt imaging, providing subsalt images of greatly improved signal-to-noise ratio (S/N) and better-balanced amplitudes compared to conventional migration methods. Most recently, the evolution of FWI from acoustic (AFWI) to elastic (EFWI) has represented another key breakthrough, yielding velocity models and FWI images with better-defined details and higher S/N, especially in salt provinces where impedance contrasts are large and elastic effects are most pronounced. Our elastic time-lag FWI (E-TLFWI), which integrates an elastic modeling engine with a time-lag cost function, has demonstrated the ability to reduce salt halos, better delineate structures around salt bodies, and enhance subsalt S/N in both velocity models and FWI images. We illustrate these improvements using two ocean-bottom node (OBN) data sets and one streamer data set. Given the proven advantages of EFWI imaging in 3D, it is natural to extend its application from 3D to 4D, particularly for subsalt 4D imaging, which often suffers from weak and imbalanced illumination and poor S/N with conventional 4D processing. The first application of E-TLFWI imaging on 4D data sets over the Atlantis Field in the Gulf of Mexico reveals clearer subsalt 4D signals and more accurate 4D responses that were not previously observed and are confirmed by both well data and production history.

Introduction

Full-waveform inversion (FWI), introduced by Lailly (1983) and Tarantola (1984), offers a natural and elegant method to automatically build earth models by inverting recorded seismic data. Despite its hopeful outlook, successful applications of FWI in regions with large impedance contrasts, such as salt, have remained challenging for several decades. Recently, however, FWI has at least partially fulfilled its promise for updating salt velocity models automatically, leading to significant improvements in subsalt imaging, even under acoustic assumptions (Michell et al., 2017; Shen et al., 2017; Zhang et al., 2018; Nolte et al., 2019; Wang et al., 2019).

Velocity model building (VMB) traditionally focuses on inverting the low-wavenumber components of the earth model, as depicted in Claerbout's diagram (Figure 1.4-3 in Claerbout, 1985). The high-wavenumber components, which are associated with reflectivity, are typically estimated using migration algorithms. These migration algorithms normally generate images using the adjoint, rather than the inverse, operator, resulting in migrated images that often suffer from illumination variations (Claerbout, 1992), particularly in subsalt regions. While least-squares migration (LSM) can partially address this issue by approximating the inverse of the linearized forward modeling operator (Baysal et al., 1983; Schuster, 1993; Nemeth et al., 1999; Wang et al., 2016), its effectiveness is limited in regions with complex geology. Recognizing that the illumination issue can be addressed more effectively by utilizing full-wavefield data, including transmission waves, primary reflections, source and receiver ghosts, and multiples, FWI imaging was proposed to achieve full-wavefield imaging through nonlinear least-squares fitting of full-wavefield data (Zhang et al., 2020; Huang et al., 2021). This demonstrates that the scope of FWI can be extended from a VMB tool to simultaneously produce both FWI velocity models and FWI images in a single inversion using raw recorded data with minimal preprocessing. This approach has not only simplified the seismic processing workflow significantly but also has generated superior images that often cannot be matched by conventional migration or LSM methods. Moreover, unlike most VMB tools that are limited to resolving low-wavenumber components, FWI can effectively capture high-wavenumber components of the subsurface velocity by progressing toward higher frequencies. This capability has been essential for the accurate focusing of complex wavefields, including multiple scattering, in FWI imaging, which requires precise kinematics and layer contrasts in the model (Wei et al., 2021).

Although acoustic FWI (AFWI) has achieved widespread success (Michell et al., 2017; Shen et al., 2017; Zhang et al., 2018; Nolte et al., 2019; Wang et al., 2019), neglecting elastic effects can lead to significant artifacts in FWI results. For example, elastic effects from large impedance contrasts blur the salt boundary in AFWI results, creating salt halos that are much wider than would be expected based on the resolution limit at the inversion frequency (Wu et al., 2022; Zhang et al., 2023). While the salt halo — manifested as a smoothing of the salt boundary — has little impact on the overall model kinematics and migration image focusing farther away from the salt, noticeable effects often can be observed around complex salt bodies, especially near steep flanks. Furthermore, the halo may hinder the direct interpretation of FWI velocity models and FWI images around salt bodies. Therefore, taking elastic effects into account in FWI becomes essential for areas with large impedance contrasts.

Manuscript received 10 January 2025; revision received 21 February 2025; accepted 5 March 2025.
[1]Viridien, Houston, Texas, USA. E-mail: zedong.wu@viridiengroup.com; zhiyuan.wei@viridiengroup.com; zhigang.zhang@viridiengroup.com; jiawei.mei@viridiengroup.com; rongxin.huang@viridiengroup.com; ping.wang@viridiengroup.com.

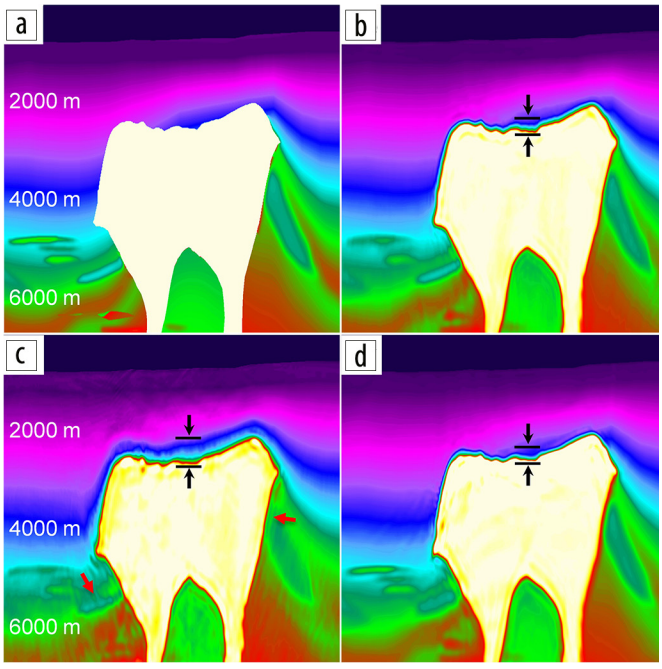

Figure 1. Synthetic tests of AFWI and EFWI using synthetic data. (a) True model, (b) A-TLFWI model using acoustic input data, (c) A-TLFWI model using elastic input data, and (d) E-TLFWI model using elastic input data.

Elastic time-lag FWI

Plessix and Krupovnickas (2021) suggest that the elastic wave equation should be used in FWI to directly account for the elastic effects, particularly for long-offset data in the presence of large impedance contrasts. Wu et al. (2022) presented elastic time-lag FWI (E-TLFWI) by combining an elastic wave modeling engine with the well-established acoustic time-lag FWI (A-TLFWI) algorithm (Zhang et al., 2018; Wang et al., 2019). In the elastic modeling engine, reflection and transmission energies at large impedance contrasts are more accurately represented in terms of both amplitude and phase, resulting in an improved match with the recorded data.

To demonstrate the benefit of E-TLFWI in the presence of large impedance contrasts, we use a synthetic data set generated from the BP 2004 velocity benchmark model (Billette and Brandsberg-Dhal, 2005), shown as the true model in Figure 1a. Figure 1b displays the inverted velocity using acoustic input data and AFWI up to 10 Hz, which produces a reasonable salt boundary and subsalt velocity. However, when we switch to elastic input data while still using AFWI (Figure 1c), a clear salt halo appears, as well as noticeable cross-cutting noise, as highlighted by the red arrows. This synthetic example suggests that the salt halo results from the elastic effects in the data at the salt boundary not being accurately modeled using an AFWI approach. In contrast, elastic FWI (EFWI) using elastic input data (Figure 1d) significantly reduces the salt halo and mitigates the cross-cutting noise in the subsalt, as observed in the AFWI results using elastic input data (Figure 1c), due to the improved data misfit and better convergence achieved through the elastic wave modeling engine.

In the following sections, we demonstrate that the same observations can be made exactly on the field data applications, where the salt halo is significantly reduced in the E-TLFWI velocity model, and the resulting FWI image demonstrates more balanced amplitudes, improved continuity, and a higher signal-to-noise ratio (S/N) compared to the acoustic counterpart. We use the Mad Dog ocean-bottom node (OBN) and Deux streamer data sets from the Gulf of Mexico (GoM), as well as the Santos Basin OBN from Brazil, to illustrate the effectiveness of E-TLFWI in improving subsalt images and compare the resulting velocities and FWI images with well data. We also use Atlantis OBN data from GoM to demonstrate the benefits of using E-TLFWI imaging for 4D monitoring. Finally, we discuss the path forward to further improve E-TLFWI results and the benefit of replacing acoustic reverse time migration (A-RTM) with elastic reverse time migration (E-RTM) to fully leverage the accuracy of the E-TLFWI velocity model, particularly when generating high-frequency stacks and gathers in a cost-efficient manner.

Mad Dog OBN data

Mad Dog is a major hydrocarbon field in the GoM, with an estimated 6 billion barrels of oil originally in place. Located in the Green Canyon protraction area about 150 miles south of New Orleans, the field lies beneath the Sigsbee Escarpment, with water depths ranging from approximately 4100 ft to more than 6000 ft. The field is situated within a large anticlinal structure in the western part of the Atwater Fold Belt, with most of it lying under an allochthonous salt canopy of varying thickness, the maximum reaching about 8000 ft.

In this study, A-TLFWI was run up to 11 Hz and E-TLFWI up to 20 Hz. Compared to A-TLFWI (Figure 2a), the E-TLFWI model better resolved the complex velocity structure (Figure 2b) and significantly enhanced the subsalt image quality (Figure 2d) when compared to the RTM image using the AFWI velocity model (Figure 2c), with much better focusing and a higher S/N. The FWI image produced by E-TLFWI revealed the compartmentalization of this area, a finding that was confirmed by a previously drilled well in the region. The improved image reduced uncertainties for future well targeting and planning (Liu et al., 2023).

The A-TLFWI model (Figure 2a) shows a large salt halo with a thickness of about 500 ft (indicated by the black bar) due to velocity smearing around the salt body. As a result, the sharp salt boundary typical of conventional salt picking was lost. The large salt halo was due to the A-TLFWI being unable to properly model the strong elastic effects around salt boundaries with large impedance contrasts, failing to focus the halo as the frequency increases. This halo rendered the A-TLFWI velocities unsuitable for pressure prediction near the salt boundary and limited the accuracy of salt depth estimation for well planning.

In contrast, E-TLFWI used an elastic wave propagation engine that better predicts phase and amplitude of the strong reflection energy at the salt boundary, thus significantly reducing the mismatch between recorded and modeled data. As a result, E-TLFWI effectively reduced the salt halo and sharpened the salt boundary (Figure 2b). The blue circle in Figure 2d highlights

a geobody in the overburden, characterized by complex sediment-salt interactions. The team struggled with imaging this feature for years and conducted numerous scenario tests with little success in the past (Liu et al., 2023).

For additional quality control of the inverted velocity, sonic logs were compared with velocity profiles extracted from both the A-TLFWI and E-TLFWI models (Figure 3). In this comparison, both models were run up to 15 Hz (A-TLFWI in yellow and E-TLFWI in red). The velocity profiles produced by E-TLFWI matched the sonic logs much more closely. The large salt halo seen in the A-TLFWI model was evident in these plots, while the E-TLFWI velocity around the salt did not suffer from this halo artifact and aligned better with the sonic logs, making it a more reliable choice for pressure prediction.

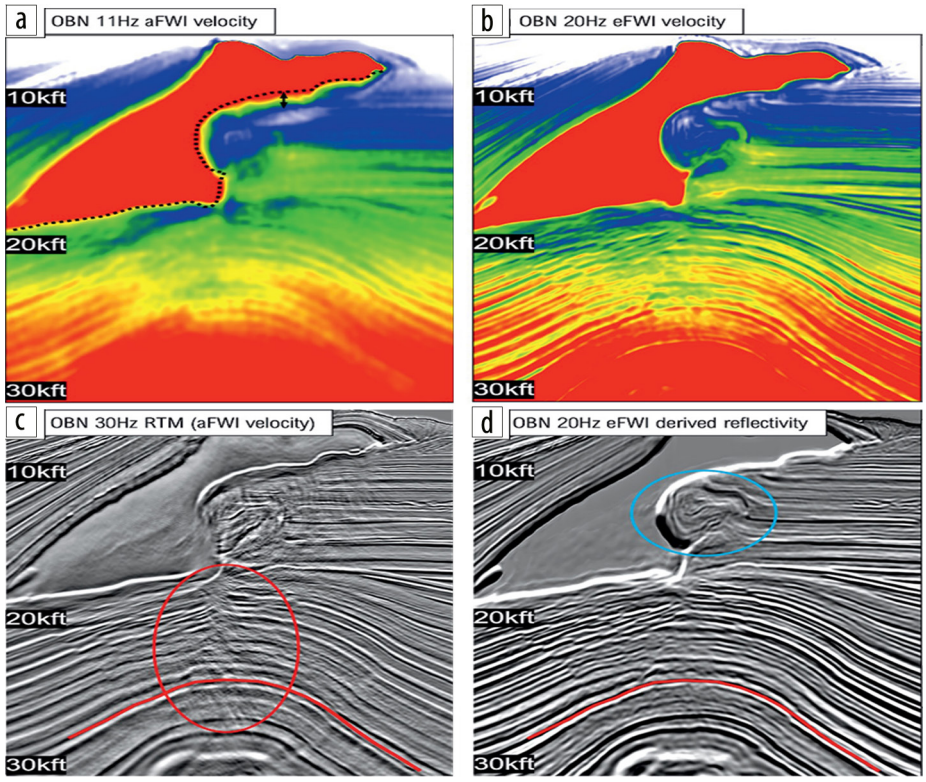

Figure 2. Section views of velocity models and corresponding images at Mad Dog. (a) OBN 11 Hz A-TLFWI velocity model, (b) OBN 20 Hz E-TLFWI velocity model, (c) 30 Hz OBN RTM full-stack image migrated with A-TLFWI model, and (d) 20 Hz E-TLFWI image. Modified from Liu et al. (2023).

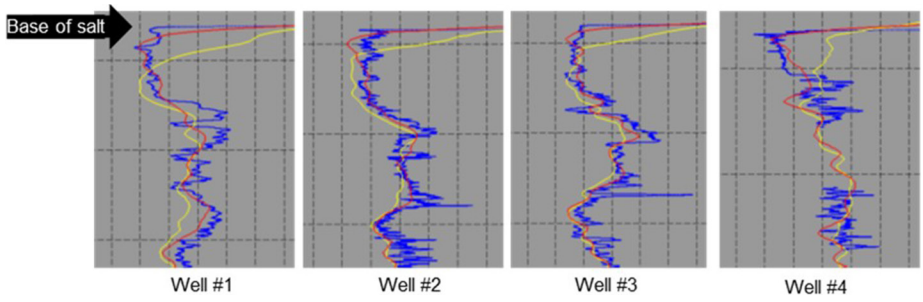

Figure 3. Velocity comparison for four wells. Sonic logs are in blue, 15 Hz E-TLFWI velocity curves are in red, and 15 Hz A-TLFWI velocity curves are in yellow. Modified from Liu et al. (2023).

Deux streamer data

The next example corresponds to an application of E-TLFWI on a full-azimuth towed-streamer data set with a maximum offset of 18 km, a data type that presents challenges for both VMB and imaging in subsalt settings compared to modern OBN acquisitions. The test focused on the Shenandoah area of Walker Ridge in the GoM, where imaging was complicated by thick salt bodies and complex subsalt structures. To improve the velocity model, several rounds of iterative salt scenarios and A-TLFWI were applied. After multiple rounds of A-TLFWI, the resulting RTM image and its corresponding FWI velocity model are shown in Figures 4a and 4b, respectively. At 8 Hz, compared to the A-TLFWI velocity model (Figure 4b), the E-TLFWI model (Figure 4d) shows reduced salt halos and better delineated structures near the salt flanks. The resulting RTM (Figure 4c), while still acoustic, was slightly improved with better focusing in the subsalt area and reduced cross-cutting noise, as highlighted by the green arrows, when using the E-TLFWI velocity model. A comparison of the A-TLFWI image (Figure 5a) with the E-TLFWI image (Figure 5b) reveals more distinct uplifts than those observed in the RTM comparison. Compared to the A-TLFWI image (Figure 5a), the E-TLFWI image (Figure 5b) exhibits better event continuity and a higher S/N, similar to the improvements seen in the OBN data examples. Even with these less favorable streamer data with limited offsets, the advantages of E-TLFWI were still evident.

Santos Basin OBN data

After presenting two field data examples from the GoM, we move to another region featuring large salt bodies in Brazil. The next test area was covered by an OBN data set with a maximum offset of 20 km in the Santos Basin offshore Brazil. Figures 6a and 6b show 30 Hz A-TLFWI and 30 Hz E-TLFWI velocity models, respectively. The E-TLFWI model exhibits sharper velocity contrasts and improved details, along with a better match with the composite log at the igneous rock interval. When compared with the well sonics (Figure 6c), the E-TLFWI model also provided a better match than the A-TLFWI model.

Figure 7 compares legacy, A-TLFWI, and E-TLFWI velocity models (Figures 7a, 7c, and 7e, respectively). The A-TLFWI enhanced the legacy velocity (Figure 7a) by capturing additional details in the subsurface (Figure 7c). Compared to the 45 Hz RTM migrated with the legacy model (Figure 7b), the 30 Hz A-TLFWI

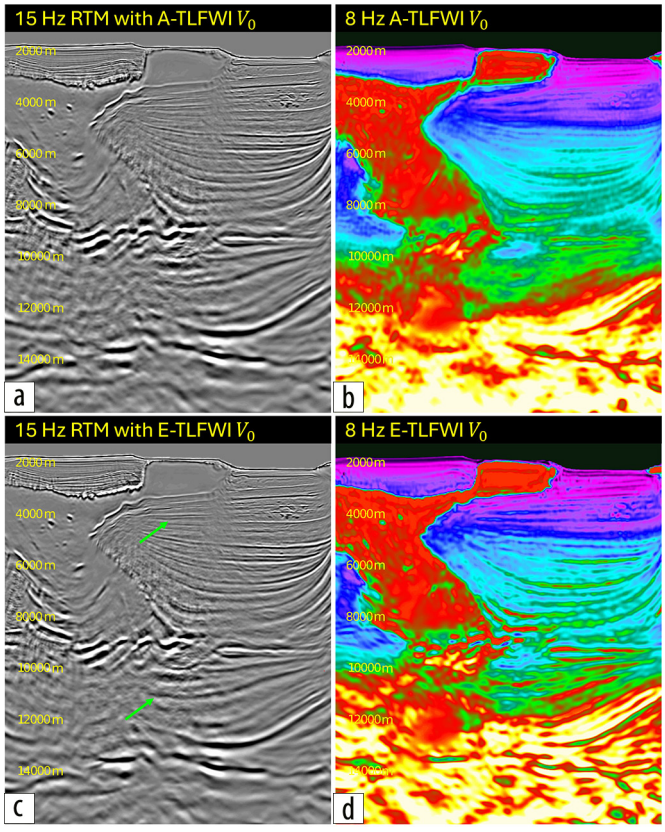

Figure 4. Velocity and imaging comparisons for Deux streamer GoM data set. (a) RTM with (b) 8 Hz A-TLFWI velocity model. (c) RTM with (d) 8 Hz E-TLFWI velocity model.

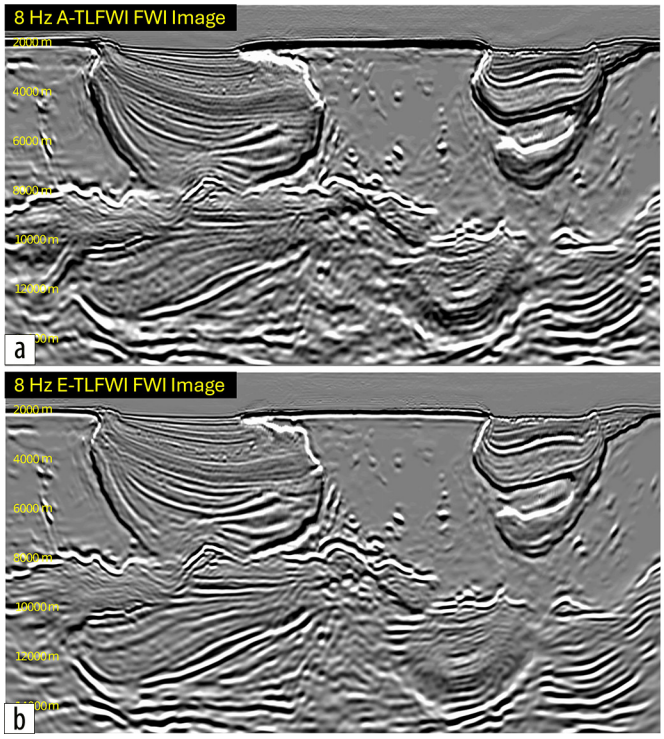

Figure 5. FWI image comparison between A-TLFWI and E-TLFWI on Deux streamer GoM data set. (a) A-TLFWI image and (b) E-TLFWI image.

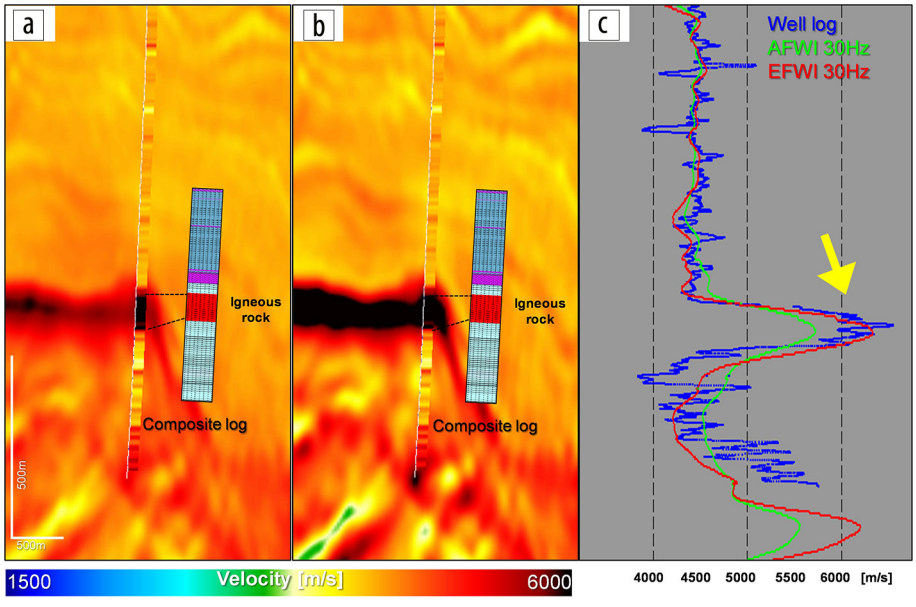

Figure 6. The E-TLFWI model at Santos Basin exhibits sharper velocity contrasts and greater details along with a better match with the composite log at the igneous rock interval. (a) 30 Hz A-TLFWI, (b) 30 Hz E-TLFWI, and (c) well sonic log comparison. Modified from Pacheco et al. (2024).

image shows much improved event continuity and resolution for the presalt events (Figure 7d). Figure 7e shows the E-TLFWI model, which has a sharper velocity with stronger contrasts in the presalt as expected from the geology of the region. However, the E-TLFWI image (Figure 7f) only exhibits a slight improvement compared to the A-TLFWI image (Figure 7d), with a sharper top of salt event and reduced halos and a slightly improved S/N in the presalt. This is likely because the salt bodies had less complexity in this area and the S/N of the A-TLFWI image at the presalt was already good. Most of the value of E-TLFWI came from the better-defined details and contrasts in the E-TLFWI velocity model. These provided more accurate information for identifying igneous and other presalt formations, as illustrated in Pacheco et al. (2024).

4D E-TLFWI imaging

The Atlantis Field is situated in the Green Canyon area of the GoM, approximately 150 miles south of New Orleans. A large portion of the field is obscured by a complex allochthonous salt body, which includes several thin salt fingers that pinch out over the crest of the reservoir. Buist et al. (2023) showed that E-TLFWI can largely reduce the salt halo observed in the A-TLFWI velocity and sharpen the velocity contrasts, improving details compared to the A-TLFWI velocity model. This resulted

in extraordinary resolution and reservoir detail in E-TLFWI images that had not been observed before at Atlantis (Buist et al., 2023). Moreover, from the structural and stratigraphic interpretation of the field using E-TLFWI images, reservoir surfaces and faults have attained improved lateral and vertical positioning in comparison to the legacy interpretation from the conventionally migrated seismic data. This improvement has led to an updated drilling target (black box) and well trajectory (blue curve), thus reducing the risk of faulting out of the reservoirs (Buist et al., 2023), as shown in Figure 8. Besides the benefits of the E-TLFWI image over the A-TLFWI image, Buist et al. (2023) also observed that the E-TLFWI velocity enhanced subsalt 4D RTM events when compared to results using the A-TLFWI velocity. As shown in the previous examples, along with many results published previously (e.g., Zhang et al., 2020; Huang et al., 2021; Wei et al., 2021; Brando et al., 2023; Hao et al., 2023; Gangopadhyay et al., 2024; Ristow et al., 2024), E-TLFWI imaging often produces superior subsalt images to RTM, especially in subsalt regions where illumination issues exist. Can E-TLFWI imaging be extended from 3D to 4D imaging to further improve the subsalt 4D signals over 4D RTM?

Different 4D FWI workflows have been proposed in the literature (e.g., Denli and Huang, 2009; Malcolm and Willemsen, 2016; Kamei and Lumley, 2017; Xue et al., 2021). For this highly repeated 4D OBN data set, we adopted a parallel 4D FWI workflow, where separate E-TLFWI applications were conducted for the baseline and monitor surveys using the Atlantis 2005 and 2022 data after 4D trace selection. We note that unlike 3D FWI cases where raw data with minimum processing are often used, processed data are used in this 4D FWI workflow to mitigate the 4D noise induced by nonrepeatable multiples and other noises between baseline and monitor data. Figure 9a shows the initial 4D E-TLFWI model, which is a smoothed version of the 25 Hz E-TLFWI model from a previous 3D imaging project. This model, derived from the 2022 OBN data, captures high-resolution details validated by well data (Buist et al., 2023; Hao et al., 2023). However, such details must be smoothed out in the starting model as we run baseline and monitor E-TLFWI from low frequencies. Figures 9b and 9c display the inverted baseline and monitor 25 Hz E-TLFWI models, which recapture those details with great consistency despite the baseline and monitor E-TLFWI being run separately, owing to the robustness of the FWI algorithm and the high level of survey repeatability. Figure 9d shows the 4D velocity difference, obtained by directly subtracting the baseline and monitor models, where production-related changes are clearly

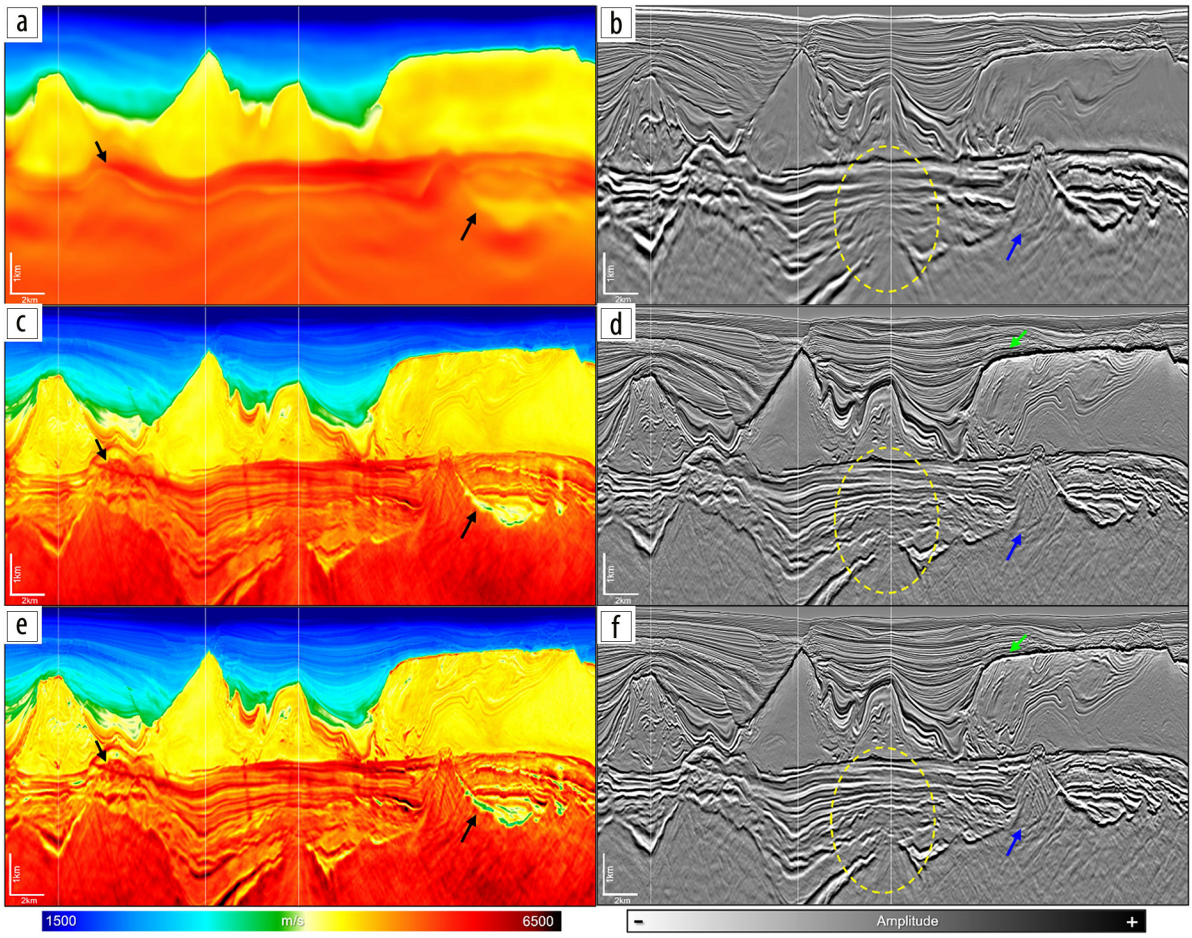

Figure 7. Comparison between legacy, A-TLFWI, and E-TLFWI velocity models and their corresponding images at Santos Basin. (a) Legacy velocity model, (b) legacy 45 Hz RTM, (c) 30 Hz A-TLFWI velocity model, (d) 30 Hz A-TLFWI image, (e) 30 Hz E-TLFWI velocity model, and (f) 30 Hz E-TLFWI image. The black arrows indicate details on the velocity model captured by A-TLFWI and enhanced by E-TLFWI compared to the legacy model. On the images, the yellow dashed area shows the region highlighting the benefits of FWI imaging compared to legacy RTM. The green arrow highlights the sharper top of salt on the E-TLFWI image, and the blue arrow indicates better defined faults on the basement. Modified from Pacheco et al. (2024).

visible (dotted ellipse). The 4D E-TLFWI image was produced by subtracting the 3D FWI images, which related to the normal derivatives of the 3D baseline and monitor E-TLFWI velocity models, respectively.

Figure 10 compares section views of 3D images of the 2022 OBN data from the 25 Hz RTM after postprocessing using the 25 Hz E-TLFWI model and the 25 Hz E-TLFWI image (Figures 10a and 10b, respectively), as well as the corresponding 4D images between the 2005 and 2022 OBN data (RTM and E-TLFWI image in Figures 10c and 10d, respectively). As shown in Figure 10a, subsalt reservoirs beneath the salt canopy were difficult to image due to poor illumination, resulting in weak amplitudes and a low S/N in the RTM image. In contrast, the 25 Hz E-TLFWI image shows more balanced amplitudes and a higher S/N (Figure 10b), revealing subsalt reservoirs that were not visible in the RTM image (circled area in Figures 10a and 10b). Similar benefits can be observed on the 4D E-TLFWI image. While the 4D RTM failed to capture 4D responses in the subsalt area (Figure 10c), the 4D E-TLFWI image clearly revealed 4D changes in the subsalt portion (Figure 10d). The hardening responses, indicated in blue, and the softening response, indicated in yellow, were supported by well data and production history.

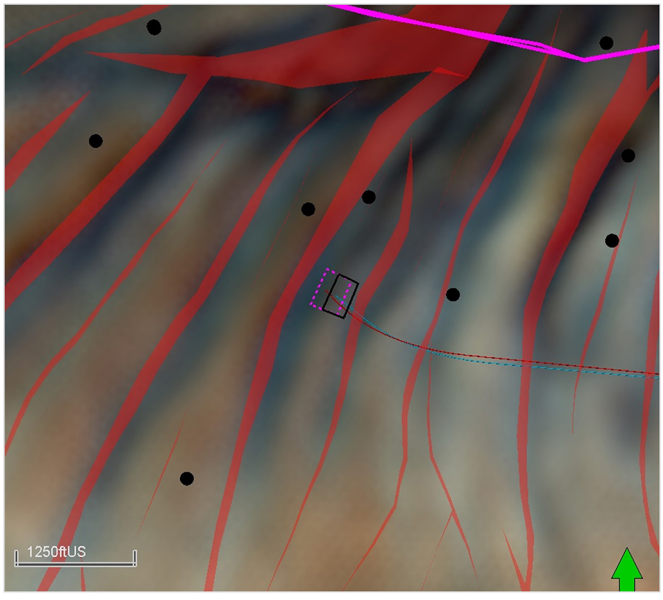

Figure 8. Updated trajectory (blue) and updated target box (black) based on E-TLFWI image observations are displayed. Legacy trajectory (red) and legacy target box (blue) are displayed for comparison. Modified from Buist et al. (2023).

More detailed interpretation and analysis of the 4D results can be found in Egbue et al. (2024).

Discussion

For all the examples shown in this paper, E-TLFWI has consistently reduced the velocity model salt halo and provided FWI images with higher S/N than A-TLFWI. The salt halo reduction can be more intuitively explained by an improved phase and amplitude match between elastically modeled data and recorded data for the strong reflection energy at the salt-sediment boundary (Wu et al., 2022). The higher S/N of EFWI images comes not only from a better match of strong reflection energy at large impedance contrasts but also from the more accurate handling of elastic energy, such as converted waves, by the elastic inversion engine, which are otherwise considered as noise in AFWI.

Despite the fact that only V_P is inverted and V_S is passively updated by an empirical V_P-V_S relationship, the benefits of E-TLFWI over A-TLFWI have been observed consistently in the salt environment for all the cases we have seen so far. We believe this is primarily due to two reasons. First, the sediment-salt boundary is very strong, making the modeling accuracy of reflection energy at this boundary critical for FWI. However, the acoustically modeled data deviate significantly from the recorded data. Therefore, introducing the elastic modeling engine with a reasonable V_S model, even if not perfectly precise, can readily produce more accurately modeled data. Second, the elastic properties of salt are relatively stable and well understood, allowing us to provide a sufficiently accurate V_S model for the critical sediment-salt interface. In some cases, where V_S exhibits abnormal behavior that cannot be ignored, a more precise V_S may be required. In such instances, we need to derive a reasonable V_S model from well data or other a priori information, if such information is available.

Another important parameter to consider is density. For the presented examples, we either used a constant density or relied on a Gardner density model. In this case, the corresponding FWI image still reflects the impedance contrast due to the density leakage, which is desired if we wish to conduct structural imaging. However, a more detailed analysis of rock properties for prospecting and reservoir assessment would require the accurate estimation of elastic parameters such as V_P, V_S, and density. Ultimately, our goal is to perform multiparameter EFWI to directly invert for V_P, V_S, and density (or other equivalent parametrizations). However, due to current algorithm and data limitations, these parameters remain strongly coupled, making it very challenging to derive

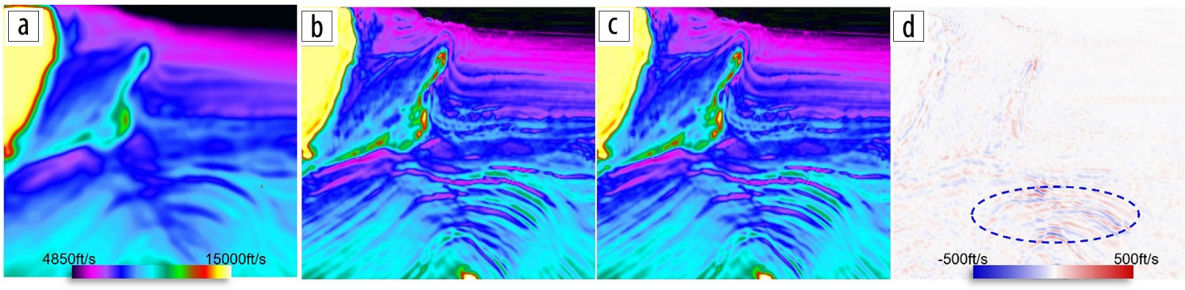

Figure 9. Section views of velocity models and differences at Atlantis. (a) Initial model for 4D E-TLFWI, (b) 25 Hz baseline E-TLFWI model, (c) 25 Hz monitor E-TLFWI model, and (d) differences between 25 Hz baseline and monitor E-TLFWI models. The model differences clearly show the production-related 4D responses. Modified from Egbue et al. (2024).

accurate V_P, V_S, and density attributes, thereby diminishing the value of multiparameter EFWI. To better separate their contributions, several areas require further investigation: (1) improving the inversion algorithm to improve separation of elastic parameters, (2) increasing constraints from multicomponent data (e.g., pressure and three-component velocity data from OBN surveys), and (3) designing sensors or surveys that provide additional constraints for key elastic parameters.

While FWI technology is continuously advancing and broadening its applications, from VMB to FWI imaging, from AFWI to EFWI, and from 3D to 4D, RTM — as the most accurate migration approach — is still an important tool for velocity validation and a needed final product in the salt environment. However, A-RTM may not fully capture the improvements made by E-TLFWI, as seen in previous examples (Huang et al., 2023), due to the inconsistencies in modeling engines between A-RTM and E-TLFWI. In regions affected by strong elastic effects, these inconsistencies may degrade A-RTM images migrated using an E-TLFWI model, diminishing or sometimes even outweighing the kinematic improvements brought by the E-TLFWI model. In contrast, E-RTM, which uses the same modeling engine as E-TLFWI, gives better results using the E-TLFWI velocity model than A-RTM using the A-TLFWI or E-TLFWI model. As demonstrated in Figure 11, E-RTM using the E-TLFWI velocity model (Figure 11f) produced the most continuous image and gathers compared to both A-RTM images in Figures 11b and 11e.

Conclusions

We have illustrated the benefits that E-TLFWI can bring for improving subsalt images. It can significantly reduce salt halos due to the elastic modeling engine providing a better match between modeled and recorded data. Additionally, E-TLFWI potentially can utilize converted waves that are otherwise considered noise and cause artifacts in A-TLFWI. These benefits enable E-TLFWI to achieve a higher S/N than

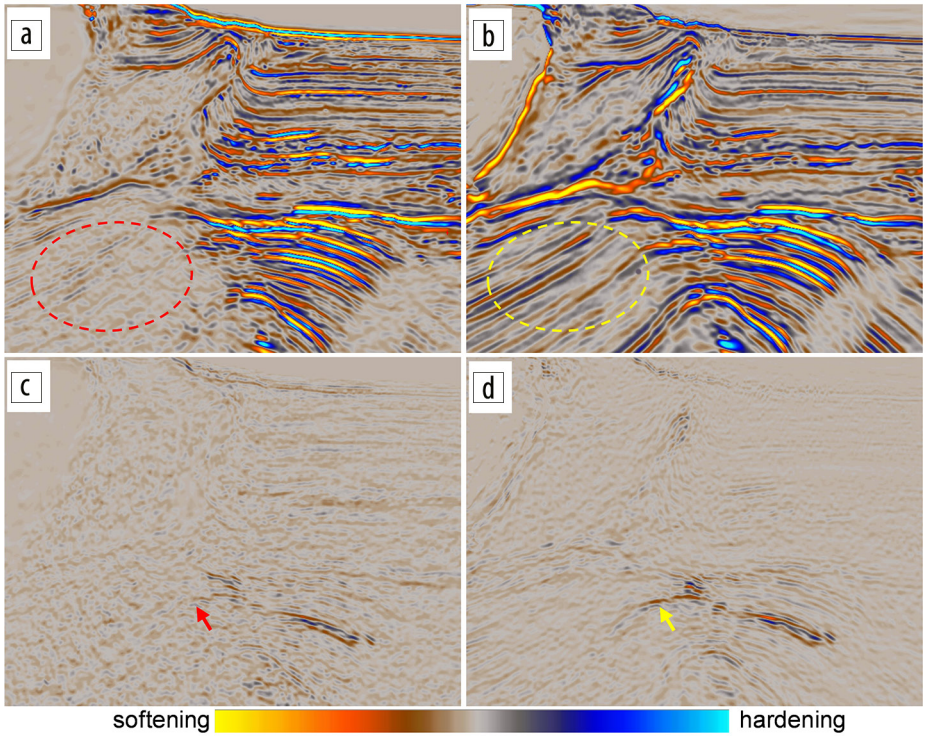

Figure 10. Section views of 3D images and 4D differences at Atlantis. (a) Postprocessed 25 Hz RTM image with 2022 OBN using the 25 Hz E-TLFWI model from the 3D project, (b) 25 Hz E-TLFWI image with 2022 OBN, (c) 25 Hz RTM 4D after postprocessing, and (d) 25 Hz 4D E-TLFWI image. The 4D E-TLFWI imaging difference shows a clearer subsalt 4D signal than the 4D RTM in the Atlantis subsalt area. Modified from Egbue et al. (2024).

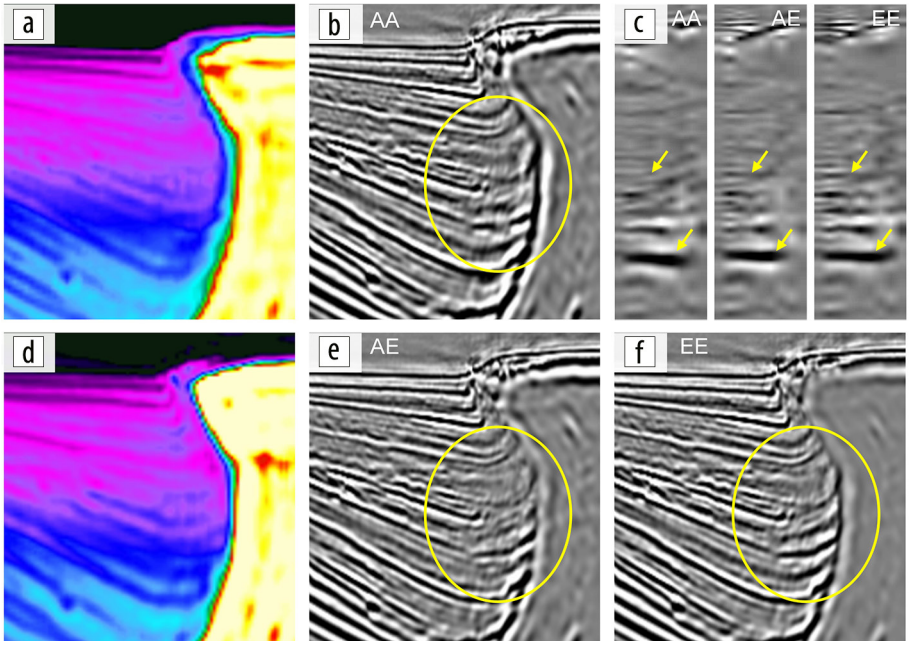

Figure 11. RTM comparison in the Walker Ridge Field with sediment-salt truncation. (a) 8 Hz A-TLFWI model, (b) 15 Hz A-RTM image with A-TLFWI model, (c) surface offset gathers (SOGs) of the three RTM images, (d) 8 Hz E-TLFWI model, (e) 15 Hz A-RTM image with E-TLFWI model, and (f) 15 Hz E-RTM image with E-TLFWI model. The location of the SOG is indicated by the red arrow in (b). In (b), (c), (e), and (f), "AA" means A-RTM with A-TLFWI model, "AE" means A-RTM with E-TLFWI model, and "EE" means E-RTM with E-TLFWI model.

A-TLFWI in velocity models and FWI images, especially in subsalt areas. We have further demonstrated that E-TLFWI imaging can be extended from 3D to 4D, which is particularly beneficial for 4D monitoring of subsalt reservoirs in poorly illuminated areas.

We have also discussed the limitations of current E-TLFWI results and the challenges associated with multiparameter EFWI, and how before we can reliably separate the key elastic attributes through multiparameter EFWI, gathers from conventional migration or FWI imaging will still be needed for gather-based elastic inversion. Finally, E-RTM, using the same elastic wave modeling engine as E-TLFWI, should be used instead of A-RTM to extract the full benefits of the E-TLFWI velocity model. TLE

Acknowledgments

We thank our various clients for the opportunities to work on their data and Viridien for permission to publish this work. We are also grateful to many Viridien colleagues for applying E-TLFWI to different data sets.

Data and materials availability

Data associated with this research are confidential and cannot be released.

Corresponding author: zedong.wu@cgg.com

References

Baysal, E., D. D. Kosloff, and J. W. C. Sherwood, 1983, Reverse time migration: Geophysics, **48**, no. 11, 1514–1524, https://doi.org/10.1190/1.1441434.

Billette, F. J., and S. Brandsberg-Dhal, 2005, The 2004 BP velocity benchmark: 67th Conference and Exhibition, EAGE, Extended Abstracts, https://doi.org/10.3997/2214-4609-pdb.1.B035.

Brando, G., B. Huard, and L. Cypriano, 2023, Imaging the presalt with elastic FWI using OBN data: Third International Meeting for Applied Geoscience & Energy, SEG/AAPG, Expanded Abstracts, 685–689, https://doi.org/10.1190/image2023-3917169.1.

Buist, S., L. Jiang, O. Egbue, D. Tebo, L. Lopez, Z. Wei, A. Hao, and C. Chen, 2023, Atlantis — 20 years of seismic innovation finally removes the shroud of mystery: The Leading Edge, **42**, no. 6, 406–413, https://doi.org/10.1190/tle42060406.1.

Claerbout, J. F., 1985, Imaging the earth's interior: Blackwell Scientific Publications Inc.

Claerbout, J. F., 1992, Earth soundings analysis: Processing versus inversion: Blackwell Scientific Publications Inc.

Denli, H., and L. Huang, 2009, Double-difference elastic waveform tomography in the time domain: 79th Annual International Meeting, SEG, Expanded Abstracts, 2302–2306, https://doi.org/10.1190/1.3255320.

Egbue, O., L. Jiang, C. Chen, S. Strauss, Z. Wu, and Z. Wei, 2024, Capturing elusive subsalt 4D signals in Atlantis Field with 4D elastic FWI imaging: Fourth International Meeting for Applied Geoscience & Energy, SEG/AAPG, Expanded Abstracts, 2580–2584, https://doi.org/10.1190/image2024-4099915.1.

Gangopadhyay, A., L. Jiang, R. Chrisman, S. Banerjee, H. Su, B. Deng, B. Bonala, and J. Mei, 2024, Improved interpretability from elastic full waveform inversion model-based seismic images revitalizes Paleogene development in the Gulf of Mexico: Fourth International Meeting for Applied Geoscience & Energy, SEG/AAPG, Expanded Abstracts, 896–900, https://doi.org/10.1190/image2024-4093609.1.

Hao, A., C. Chen, Z. Wei, J. Mei, L. Jiang, S. Buist, O. Egbue, L. Lopez and D. Tebo, 2023, Meeting the imaging challenges at Atlantis with high-frequency elastic FWI: Third International Meeting for Applied Geoscience & Energy, SEG/AAPG, Expanded Abstracts, 615–619, https://doi.org/10.1190/image2023-3911776.1.

Huang, H., Z. Wu, X. Xiao, Z. Zhang, and P. Wang, 2023, The need of elastic RTM for elastic FWI models: Third International Meeting for Applied Geoscience & Energy, SEG/AAPG, Expanded Abstracts, 1441–1445, https://doi.org/10.1190/image2023-3914419.1.

Huang, R., Z. Zhang, Z. Wu, Z. Wei, J. Mei, and P. Wang, 2021, Full-waveform inversion for full-wavefield imaging: Decades in the making: The Leading Edge, **40**, no. 5, 324–334, https://doi.org/10.1190/tle40050324.1.

Kamei, R., and D. Lumley, 2017, Full waveform inversion of repeating seismic events to estimate time-lapse velocity changes: Geophysical Journal International, **209**, no. 2, 1239–1264, https://doi.org/10.1093/gji/ggx057.

Lailly, P., 1983, The seismic inverse problem as a sequence of before stack migrations, *in* J. B. Bednar, E. Robinson, and A. Weglein, eds., Conference on inverse scattering—Theory and application, 206–220.

Liu, H., F. Rollins, K. Pratt, E. Da Silva, N. Mootoo, T. Yang, D. Ren, F. Gao, and J. Mei, 2023, Solving Mad Dog subsalt imaging in two decades: From WATS to OBN to elastic FWI: The Leading Edge, **42**, no. 6, 398–405, https://doi.org/10.1190/tle42060398.1.

Malcolm, A., and B. Willemsen, 2016, Rapid 4D FWI using a local wave solver: The Leading Edge, **35**, no. 12, 1053–1059, https://doi.org/10.1190/tle35121053.1.

Michell, S., X. Shen, A. Brenders, J. Dellinger, I. Ahmed, and K. Fu, 2017, Automatic velocity model building with complex salt: Can computers finally do an interpreter's job?: 87th Annual International Meeting, SEG, Expanded Abstracts, 5250–5254, https://doi.org/10.1190/segam2017-17778443.1.

Nemeth, T., C. Wu, and G. T. Schuster, 1999, Least-squares migration of incomplete reflection data: Geophysics, **64**, no. 1, 208–221, https://doi.org/10.1190/1.1444517.

Nolte, B., F. Rollins, Q. Li, S. Dadi, S. Yang, J. Mei, and R. Huang, 2019, Salt velocity model building with FWI on OBN data: Example from Mad Dog, Gulf of Mexico: 89th Annual International Meeting, SEG, Expanded Abstracts, 1275–1279, https://doi.org/10.1190/segam2019-3216777.1.

Pacheco, G., A. Araújo, D. Costa, K. Pereira, and L. Cypriano, 2024, Detecting igneous rocks in the presalt with elastic FWI: Fourth International Meeting for Applied Geoscience & Energy, SEG/AAPG, Expanded Abstracts, 901–905, https://doi.org/10.1190/image2024-4099750.1.

Plessix, R.-E., and T. Krupovnickas, 2021, Low-frequency, long-offset elastic waveform inversion in the context of velocity model building: The Leading Edge, **40**, no. 5, 342–347, https://doi.org/10.1190/tle40050342.1.

Ristow, J. P., D. Lanznaster, and F. Jouno, 2024, Advances in OBN imaging for pre-salt fields: 85th Conference and Exhibition, EAGE, Extended Abstracts, https://doi.org/10.3997/2214-4609.2024101421.

Schuster, G. T., 1993, Least-squares cross-well migration: 63rd Annual International Meeting, SEG, Expanded Abstracts, 110–113, https://doi.org/10.1190/1.1822308.

Shen, X., I. Ahmed, A. Brenders, J. Dellinger, J. Etgen, and S. Michell, 2017, Salt model building at Atlantis with full waveform inversion: 87th Annual International Meeting, SEG, Expanded Abstracts, 1507–1511, https://doi.org/10.1190/segam2017-17738630.1.

Tarantola, A., 1984, Inversion of seismic reflection data in the acoustic approximation. Geophysics, **49**, no. 8, 1259–1266, https://doi.org/10.1190/1.1441754.

Wang, P., A. Gomes, Z. Zhang, and M. Wang, 2016, Least-squares RTM: Reality and possibilities for subsalt imaging: 86th Annual International Meeting, SEG, Expanded Abstracts, 4204–4209, https://doi.org/10.1190/segam2016-13867926.1.

Wang, P., Z. Zhang, J. Mei, F. Lin, and R. Huang, 2019, Full-waveform inversion for salt: A coming of age: The Leading Edge, **38**, no. 3, 204–213, https://doi.org/10.1190/tle38030204.1.

Wei, Z., J. Mei, Z. Wu, Z. Zhang, R. Huang, and P. Wang, 2021, Unlocking unprecedented seismic resolution with FWI imaging: 82nd Conference and Exhibition, EAGE, Extended Abstracts, https://doi.org/10.3997/2214-4609.202113217.

Wu, Z., Z. Wei, Z. Zhang, J. Mei, R. Huang, and P. Wang, 2022, Elastic FWI for large impedance contrasts: Second International Meeting for Applied Geoscience & Energy, SEG/AAPG, Expanded Abstracts, 3686–3690, https://doi.org/10.1190/image2022-w17-02.1.

Xue, Z., Z. Zhang, P. Wang, and J. Cai, 2021, Joint time-lapse full-waveform inversion with a time-lag cost function: First International Meeting for Applied Geoscience & Energy, SEG/AAPG, Expanded Abstracts, 3464–3468, https://doi.org/10.1190/segam2021-3594752.1.

Zhang, Z., J. Mei, F. Lin, R. Huang, and P. Wang, 2018, Correcting for salt misinterpretation with full-waveform inversion: 88th Annual International Meeting, SEG, Expanded Abstracts, 1143–1147, https://doi.org/10.1190/segam2018-2997711.1.

Zhang, Z., Z. Wu, Z. Wei, J. Mei, R. Huang, and P. Wang, 2020, FWI imaging: Full-wavefield imaging through full-waveform inversion: 90th Annual International Meeting, SEG, Expanded Abstracts, 656–660, https://doi.org/10.1190/segam2020-3427858.1.

Zhang, Z., Z. Wu, Z. Wei, J. Mei, R. Huang, and P. Wang, 2023, Enhancing salt model resolution and subsalt imaging with elastic FWI: The Leading Edge, **42**, no. 3, 207–215, https://doi.org/10.1190/tle42030207.1.